5-2013

Noninvasive Spatial Metrology of Single-Atom Devices

Fahd A. Mohiyaddin
University of New South Wales

Rajib Rahman
Sandia National Laboratory

Rachpon Kalra
University of New South Wales

Gerhard Klimeck
Network for Computational Nanotechnology, Birck Nanotechnology Center, Purdue University, gekco@purdue.edu

Lloyd C. L. Hollenberg
University of Melbourne

See next page for additional authors

Authors

Fahd A. Mohiyaddin, Rajib Rahman, Rachpon Kalra, Gerhard Klimeck, Lloyd C. L. Hollenberg, Jarryd J. Pla, Andrew S. Dzurak, and Andrea Morello

Noninvasive Spatial Metrology of Single-Atom Devices

Fahd A. Mohiyaddin,*[,†] Rajib Rahman,[‡,⊥] Rachpon Kalra,[†] Gerhard Klimeck,[§] Lloyd C. L. Hollenberg,[‖] Jarryd J. Pla,[†] Andrew S. Dzurak,[†] and Andrea Morello*[,†]

[†]Centre for Quantum Computation and Communication Technology, School of Electrical Engineering and Telecommunications, University of New South Wales, Sydney NSW 2052, Australia

[‡]Advanced Device Technologies, Sandia National Laboratories, Albuquerque, New Mexico 87185, United States

[§]Network for Computational Nanotechnology, Purdue University, West Lafayette, Indiana 47907, United States

[‖]Centre for Quantum Computation and Communication Technology, School of Physics, University of Melbourne, Melbourne VIC 3010, Australia

Ⓢ *Supporting Information*

ABSTRACT: The exact location of a single dopant atom in a nanostructure can influence or fully determine the functionality of highly scaled transistors or spin-based devices. We demonstrate here a noninvasive spatial metrology technique, based on the microscopic modeling of three electrical measurements on a single-atom (phosphorus in silicon) spin qubit device: hyperfine coupling, ground state energy, and capacitive coupling to nearby gates. This technique allows us to locate the qubit atom with a precision of ±2.5 nm in two directions and ±15 nm in the third direction, which represents a 1500-fold improvement with respect to the prefabrication statistics obtainable from the ion implantation parameters.

KEYWORDS: ^{31}P donors in Si, quantum computing, ion implantation, donor location uncertainty, nanoelectronic modeling, triangulation
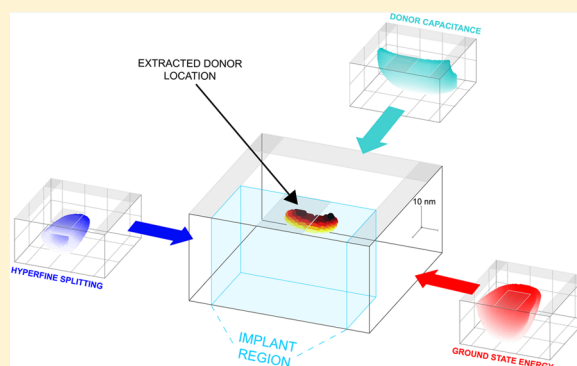
The ability to place and control individual dopant atoms in semiconductor nanostructures is paving the way to exciting and novel device functionalities.[1] For classical but highly miniaturized electronic devices, it is well established that the number and location of individual dopants has tangible effects on the performance of ultrasmall silicon transistors.[2−4] The pursuit of "deterministic doping" constitutes an important part of the effort toward further scaling of silicon chips.[5] At the extreme limit where a single dopant atom determines the device functionality, it is now possible to realize "single-atom transistors".[6−8]

Beyond classical nanoelectronic devices, single dopant atoms in silicon have been proposed as an excellent physical platform to encode and manipulate quantum information, either in the spin[9−12] or in the charge[13] degree of freedom. Indeed, the single-shot readout[14] and the coherent control[15] of a single-atom spin qubit in a silicon metal−oxide−semiconductor (MOS) structure have been recently demonstrated, as well as the control of the charge states of donor pairs.[16,17]

While great progress is being made on the atomically precise positioning of single atoms by scanning probe techniques,[8,18] ion implantation[19] remains the leading method to introduce dopants in semiconductor nanostructures in industry as well as in basic research. The inherent limitation of ion-implanted devices at the single-atom level is the straggle in the final position of the atom.[20] While this can be mitigated in part by using very low implantation energies, it is generally the case that only a probabilistic description of the final atom position can be given, using Monte Carlo techniques.[21] Therefore, techniques that accurately reveal (postfabrication) the position of an implanted dopant are crucial to inform further developments in single-atom nanoelectronic devices. Scanning probe techniques can sometimes be used to accurately locate a dopant,[1] but most often it is necessary to resort to invasive methods such as atom-probe tomography,[22] which destroys a fully functional device in the process. Moreover, in the presence of multiple dopants, the above techniques do not allow to identify which specific dopant is responsible for the observed single-atom effects. This calls for a noninvasive technique that can successfully pinpoint the location of dopants that influence the device behavior, and hence provide real-time feedback to an experiment.

Here, we present a novel modeling protocol that allows us to locate a deliberately implanted P donor in a silicon MOS spin qubit device.[23] Our non-invasive spatial metrology method enables a triangulation of the donor position which narrows the
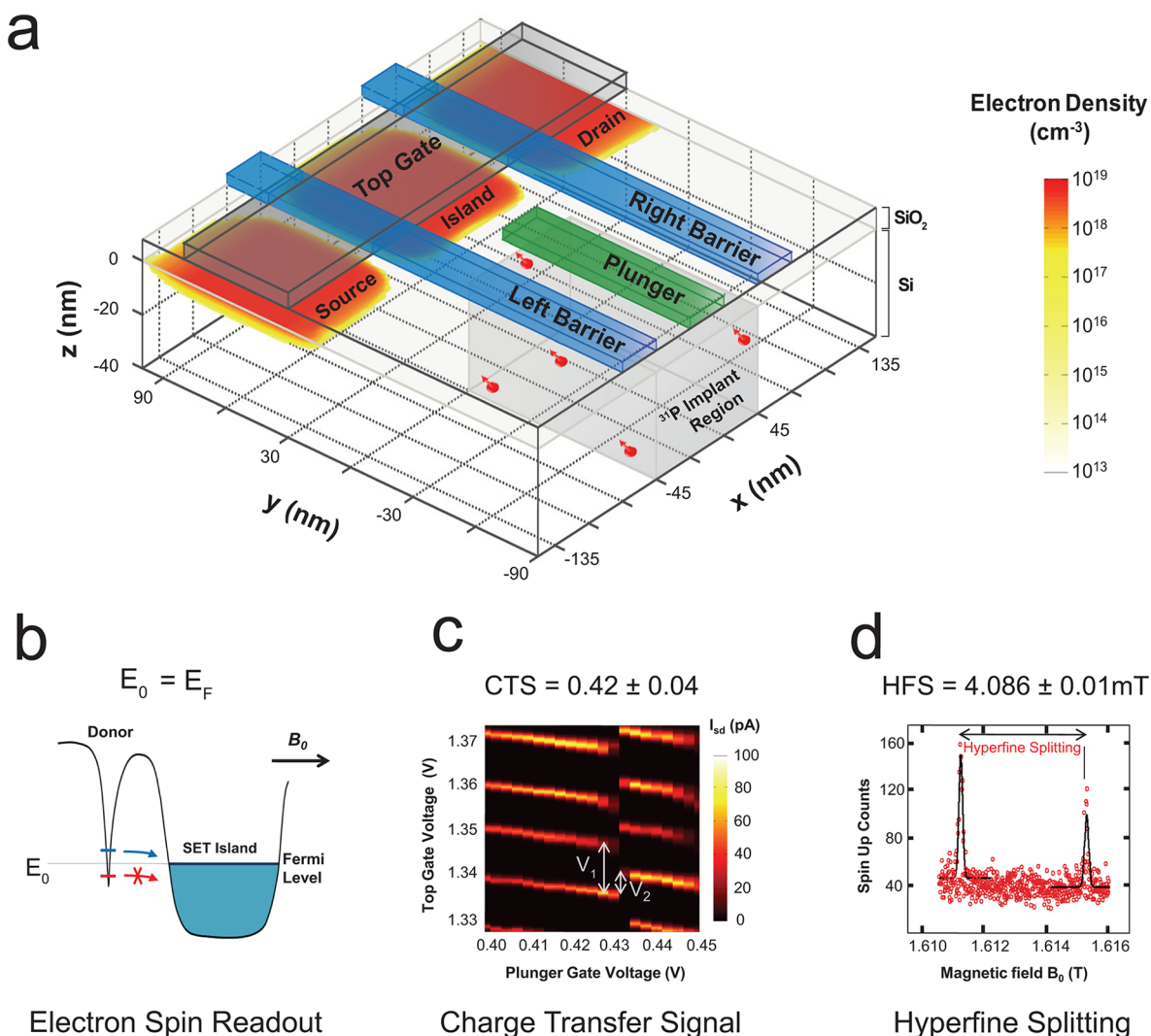
Figure 1. (a) Schematic of the spin qubit device. The electrostatic gates induce and confine electrons underneath the Si/SiO$_2$ interface. The electron density indicated in red-yellow scale highlights the position of the SET island with respect to the implant region and metallic gates. (b) Conduction band profile for the spin readout criterion, where the donor ground state is tuned in resonance with the Fermi level of SET island. (c) Charge stability diagram with transitions arising from electron tunneling between the donor and the SET island. The experimental values of voltages on the top and plunger gates shown in the figure, as well the voltages on the left and right barrier gates (0.65 V), were used to calculate the potential energy and electric field profiles. (d) Electron spin resonance spectra, showing two resonance peaks separated by the contact hyperfine splitting.

possible locations to a volume 1500 times smaller than what could have been predicted by prefabrication statistical methods. The triangulation is obtained by combining three different techniques, each one predicting a locus of donor locations compatible with a measurable physical property of the system: (i) A classical, finite-elements electrostatic simulation to match the ground state energy of the donor-bound electron; (ii) A quantum-mechanical tight-binding model[24,25] for the wave function of the donor-bound electron to match the Stark-shift of the hyperfine coupling;[26,27] (iii) A geometric capacitance extraction method[28] to match the measured capacitive coupling between the donor and the surrounding electrodes.

The schematic of the experimental device is displayed in Figure 1a. A single-electron transistor (SET) is formed under the Si/SiO$_2$ interface, by appropriate gate biasing of the metallic gates. The qubit is an individual phosphorus donor with both capacitive and tunnel coupling to the SET island. The donor under study is one of many (~16 maximum likelihood, from Poisson statistics) P atoms implanted in a 90 × 90 nm^2

window. For electron spin readout, the donor electron ground state energy is tuned in resonance with the Fermi Level of the SET island (referred to as "spin readout criterion"), as shown in Figure 1b. In an externally applied magnetic field B_0, the Zeeman splitting between the spin states results in preferential tunneling[14] of the donor spin-up electron into the island. The SET is tuned such that the spin-dependent donor ionization results in a large current, whereas no current flows while the donor is neutral (Coulomb blockade). For $B_0 = 0$, charge transitions are observed in the charge stability diagram (Figure 1c), arising from tunneling of the donor electron to the island. The transitions are characterized by the charge transfer signal (CTS)[23] $\Delta q/e = V_2/V_1 = 0.42$, where V_1 is the SET Coulomb spacing, and V_2 is the shift in the Coulomb peaks caused by donor ionization. $\Delta q/e$ also corresponds to the ratio of capacitances C_m/C_Σ, where C_m is the mutual capacitance between the donor and the island, while C_Σ is the total capacitance of the donor, including its self-capacitance and mutual capacitances to various gates and the SET island.

A microwave transmission line fabricated on the chip[29] (not included in Figure 1a) generates an oscillating magnetic field B_1 which enables electron spin control. Electron spin resonance (ESR) measurement results are plotted in Figure 1d and show two resonant peaks dependent on the state of the ^{31}P nuclear spin. The two peaks are separated by the contact hyperfine splitting (HFS), which takes the value of 4.086 mT in the experiment.[30] Because of the strong electric fields in the nanostructure, this value is Stark-shifted from the value of 4.2 mT observed in bulk samples.[31] In the remainder of this paper, we will sequentially address the simulation strategy and results of the hyperfine splitting, the spin readout criterion, the charge transfer signal, and their triangulation.

The spin Hamiltonian of a donor electron spin **S** and nuclear spin **I** in an applied electric field ε and magnetic field $\mathbf{B}_0$ is given by:

$$H = g_e(\varepsilon)\mu_B \mathbf{S} \cdot \mathbf{B}_0 - g_n \mu_n \mathbf{I} \cdot \mathbf{B}_0 + A(\varepsilon)\mathbf{I} \cdot \mathbf{S} \quad (1)$$

The first and second terms in eq 1 are electronic and nuclear Zeeman terms, the third term is the contact hyperfine interaction between the two spins, $g_e(\varepsilon)$[32] and g_n are the electron and nuclear gyromagnetic ratios, and μ_B and μ_n are the Bohr and nuclear magnetons, respectively. The contact hyperfine interaction is expressed as $A(\varepsilon) = (8\pi/3)g_e g_n \mu_B \mu_n |\psi(r_0,\varepsilon)|^2$, where $|\psi(r_0,\varepsilon)|^2$ is the probability density of the electron wave function evaluated at the donor site r_0. In realistic devices, $|\psi(r_0,\varepsilon)|^2$ is distorted from the bulk value $|\psi(r_0,0)|^2$, resulting in a Stark shift of the HFS. Hence, to electrostatically model the HFS, it is essential to obtain the potential profile in the nanostructure and hence the electric fields, to be able to estimate the distortion of the donor electron wave function.

The software ISE-TCAD,[33] a finite-element Poisson equation solver, is used to obtain the potential profile taking into account the exact geometry of the device. In addition, the simulated threshold voltage in the model was calibrated to the experimental value of 0.7 V, by addition of interface charges with charge density $Q_{ox} = -3.4 \times 10^{11}$ cm^{-2} at the Si/SiO$_2$ boundary. This type of a-posteriori estimate of the fixed interface charge density is well established in the modeling of MOSFET structures. The calculated charge density is also consistent with estimates from deep level transient spectroscopic measurements.[34] The model also captures the effect of ionized donor potentials, by including a uniform positive charge density (4.63×10^{16} cm^{-3}) corresponding to the remaining 15 ionized donors in the implant region. We have also performed analysis for scenarios without ionized donors. The shift in donor locations, arising from the presence of ionized donors is by about 5 nm in the y-direction, and is comparable to the resulting donor location uncertainty obtained after modeling (discussed further below). This necessitates the inclusion of ionized donors in the TCAD model. The donor is modeled as a Coulomb potential superimposed on the TCAD potential profile, with an on-site truncation value calibrated[27,35] to obtain the bulk binding energy (45.6 meV) for ^{31}P donors in silicon. The wave functions for the complete potential profile are then obtained by solving the full atomistic tight-binding Hamiltonian with Nano Electronic MOdeling 3D (NEMO 3D) tool.[24,25] The tight-binding model used here employs a 20-band sp^{3}d^{5}s* nearest neighbor Hamiltonian, where wave functions are expressed with a linear combination of atomic orbitals. The hyperfine splitting relative to the bulk value is given by[27,36]

$$\frac{A(\varepsilon)}{A(0)} = \frac{|\psi(r_0, \varepsilon)|^2}{|\psi(r_0, 0)|^2} \quad (2)$$

The electric field dependence of the HFS for a bulk donor was investigated previously using uniform fields in tight-binding,[27] and agreed well with ESR measurements on bulk donor ensembles.[26] However, the calculation of the HFS in a nanoscale device must account for significant variations of the electric field within the donor Bohr radius, arising from the gates and ionized donors, and also due to proximal heterointerfaces. Hence, a realistic potential and electric field profile from TCAD is essential to model the experiments.

The magnitude of the electric field along a device slice is shown in Figure 2a. The inset of Figure 2a shows the ratio of
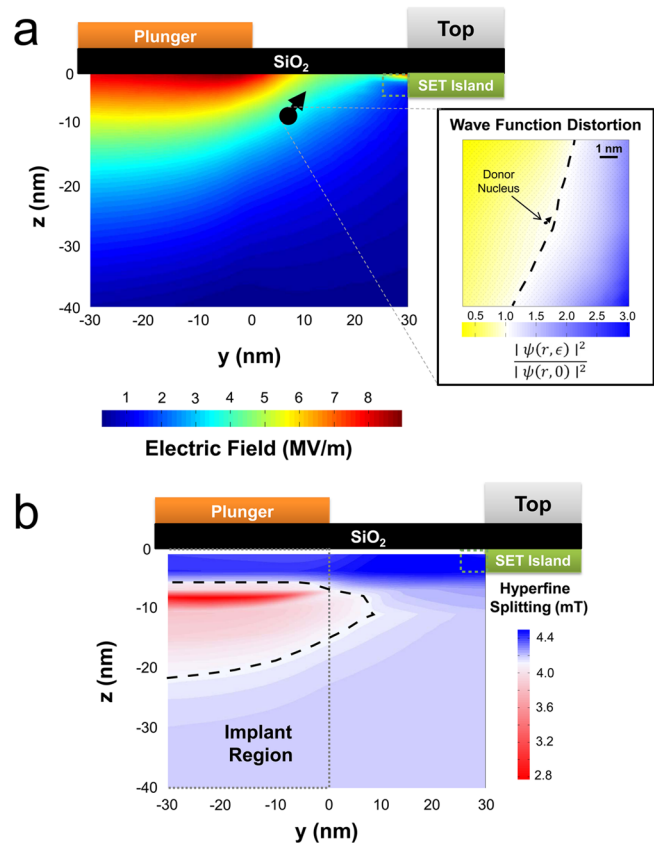

Figure 2. (a) Electric fields in a device cross section (yz-plane) cut through the center of the plunger gate. Inset: Electric-field-induced distortion of the electron probability density for a donor positioned at a specific lattice site $r_0 = (0, 7.96, -9.86)$. (b) Hyperfine splitting, Stark-shifted from the bulk value, along the yz-plane. The dashed green line represents the amount by which the SET island extends beyond the lithographic dimension of the top gate. The dotted gray line represents the approximate boundary of the implant region in the y- and z-directions.

electron probability densities for a donor located at a specific lattice site r_0, and for a bulk donor. As a consequence of the direction of the electric fields in the vicinity of the donor, the electron probability density is not only pushed toward the direction of the SET island, but also away from the Si/SiO$_2$ interface. Noticeable probability density distortion for the donor at r_0 is apparent from the inset, and results in a significant Stark shift of the contact HFS.

Figure 2b depicts the contact term of the HFS for various donor positions r_0 along the device slice. This exploration required about 600 independent atomistic NEMO-3D calculations for as many different donor positions. The map of HFS can be divided into three regions, corresponding to deep ($z < -25$ nm), intermediate depth (-25 nm $< z < -5$ nm) and very shallow ($z > -5$ nm) donors. The Stark shift is small for deep donors, with HFS close to the bulk value in electric fields lower than 1 MV/m. For intermediate depth donors, the electron probability density at r_0 is severely reduced by the large electric field, resulting in hyperfine splittings as small as 2.8 mT. The proximity of the Si/SiO$_2$ interface to the donor also influences HFS in addition to the electric field. The abrupt potential barrier modifies the wave function confinement, and hence different HFS are noticed for donors along iso-electric field lines. Additionally, the potential barrier tends to confine the electron probability density more than the bulk, thereby allowing values of the HFS beyond 4.2 mT for very shallow donors, despite the large electric field. This increase has been previously reported and analyzed with the help of first-order perturbation theory.[27] As a consequence of the variation of local electric fields and the presence of the Si/SiO$_2$ interface, the locus of donor locations compatible with the experimental HFS value of 4.086 mT takes the shape of the irregular semiellipsoid represented by the white contour in Figure 2b.

To simulate the spin readout criterion, we map out the potential energy of the system, for the set of gate voltages applied in experiment. TCAD serves this purpose by computing the conduction band profile, E_c. The TCAD map of E_c, with the Fermi level E_F set as the reference zero energy, is plotted in Figure 3a. The conduction band tends to rise in energy toward the direction of the plunger gate, since the top and plunger gates are biased at high and low positive gate voltages, respectively. The SET island extends slightly beyond the lithographic dimensions of the top gate, due to the lowering of conduction band below the Fermi level (green region in Figure 3a). By integrating the electron density in Figure 1a, 93 electrons were estimated to be present in the SET island during spin readout. The white contour in Figure 3a denotes locations where the TCAD conduction band energy is equal to the bulk binding energy of the donor. We assume that the spin readout criterion is fulfilled at these locations, since the donor ground state E_0 aligns close to E_F. The validity of the above assumption rests on the observation that the variation of E_c in Figure 3a is much larger than the modification of donor ground state binding energy by Stark shift and hybridization with the island (<1 meV as shown in the Supporting Information). This allows us to derive another donor locus consistent with the implantation region to narrow down the location of the donor qubit.

For the estimation of the charge transfer signal, we utilize the capacitance extraction software FASTCAP.[28] We note that FASTCAP has been used successfully to predict the experimental charge stability diagram of a donor-based double quantum dot fabricated by scanning probe techniques,[37] where the location of the donors is accurately known. This provides great confidence that the method can be used in reverse, that is, to predict the donor location from an experimental charge stability diagram. In FASTCAP, the donor is represented as a conducting sphere with radius $a_B = 2.5$ nm, where a_B is the Bohr radius of a ^{31}P donor electron in silicon. We note that the CTS calculated from FASTCAP is largely insensitive to small modifications of the donor size and shape. The SET island is
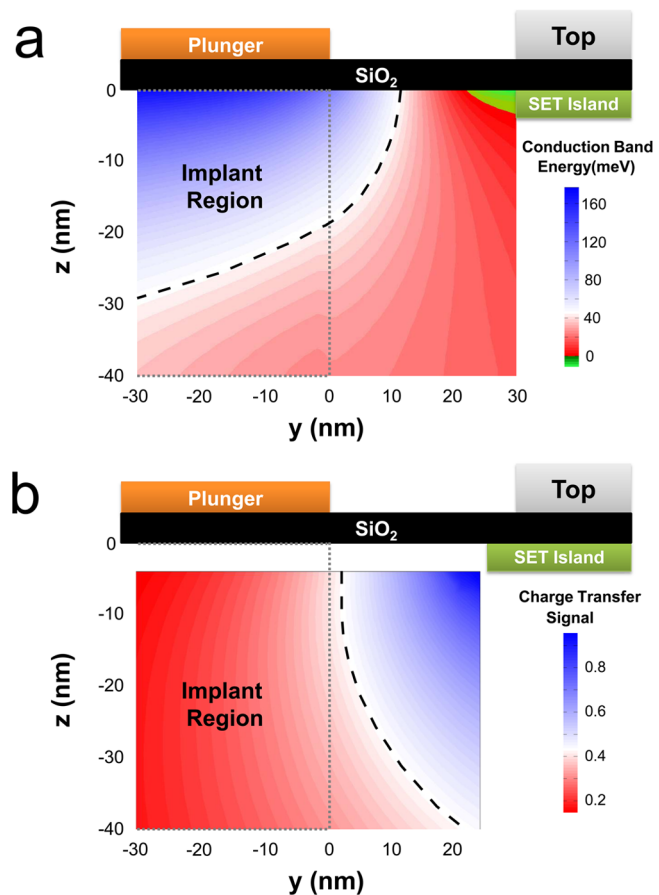

Figure 3. (a) TCAD map of the conduction band profile along the yz slice. The white regions illustrate the positions where the spin readout criterion is fulfilled. (b) Charge transfer signal computed from mutual capacitances in the nanostructure by FASTCAP.[28]

modeled as a conducting cuboid with dimensions consistent with the size of the island obtained from TCAD. Figure 3b is a plot of the CTS for donors positioned along a device slice. The trends in Figure 3b are intuitive with reduced contribution of C_m on C_Σ for donors far away from the SET and vice versa. From this data, we obtain a third donor locus corresponding to the experimental value of $\Delta q/e = 0.42$.

We now combine our results in three dimensions in Figure 4a, where the three shells correspond to donor positions satisfying the experimental criteria individually. The largest relative error, 9.5%, comes from the charge transfer signal $\Delta q/e = 0.42 \pm 0.04$, which is extracted from the three charge transitions shown in Figure 1c. A margin of 1 meV has been assumed on either side of the bulk binding energy for the spin readout criterion, to take into account thermal electron excitations and small changes in binding energy. For the hyperfine splitting, the error bar is ± 0.01 mT from the spin resonance experiment. The three parameters are independent of each other and strongly dependent on the donor position, as observed in Figures 2 and 3. In Figure 4b, we present the intersection of the three possible donor loci. The donor locations compatible with all the three criteria occupy a volume of 215 nm^3, which is ~1500 times smaller than the volume of the donor implant region in Figure 1a. In particular, we find that the lateral displacement of the donor with respect to the edge of the top gate is 26.5 ± 2.5 nm, while its depth below the Si/SiO$_2$ interface is 13.5 ± 2.5 nm. The lateral displacement
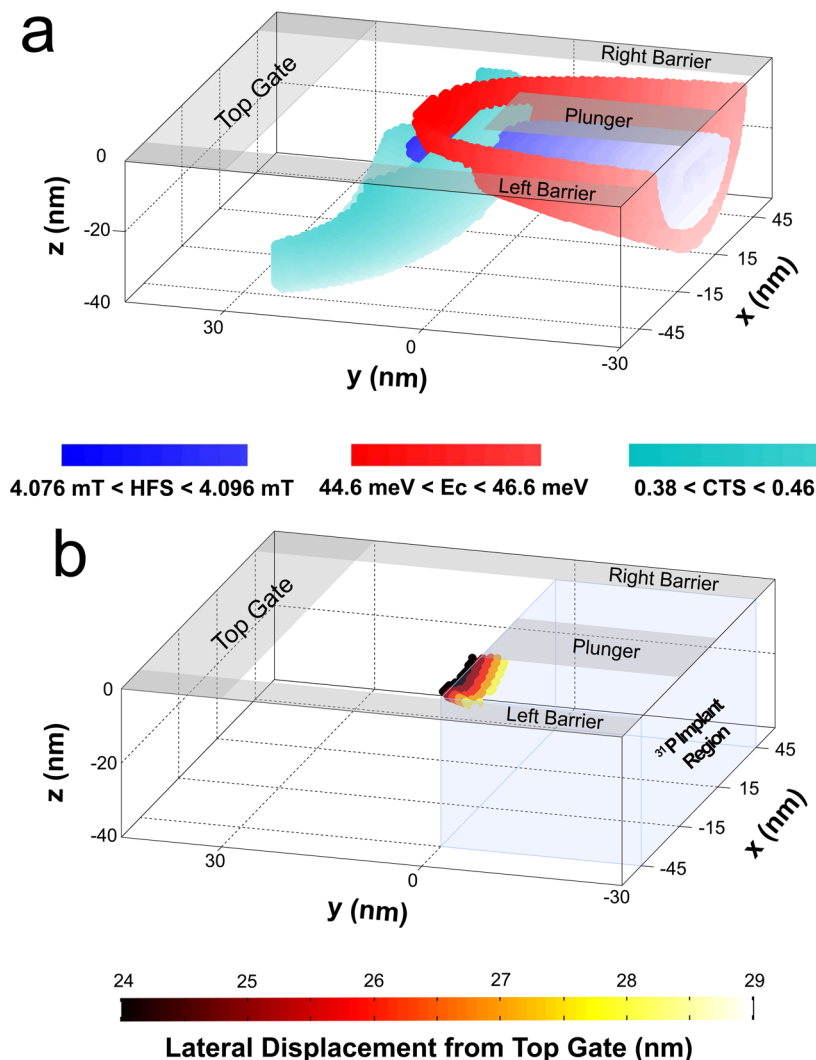
Figure 4. (a) The 3D map of donor locations compatible with the experimental hyperfine splitting (blue), spin readout criterion (red), and charge transfer signal (turquoise). (b) Possible locations of the qubit in the nanostructure obtained by the intersection of the three curves in panel a.

suggests that the donor is just outside the boundary of the implant region in the y-direction. This may be attributed to donor straggle[20] and misalignment of the implant window during fabrication. The depth implies that the implanted donor traveled 21.5 ± 2.5 nm through the 8 nm oxide and silicon before coming to rest, which is perfectly compatible with the expected implantation depths at 14 keV acceleration energy.[19] We stress that the intersection of the three independent shells in a small region compatible with the a-priori ion-implanted volume is strikingly nontrivial. This is a strong validation that our electrostatic model with uniform charge densities accurately describes the experimental solid-state environment of the donor in the nanostructure.

The volume of the implant region in the device studied here is rather large due to the choice of implanting more than one donor, and subsequently selecting one with optimal coupling. However, even if a counted single-atom implantation[19] with minimal size of the implant aperture (~10 nm) had been adopted, statistical preprocessing techniques[21] would still only locate the donor to within precisions of the order of ±10 nm,[20] due to donor straggle. The precision in the y- and z-direction obtained by our metrology technique is already much better than the above value, despite the large experimental error bar in

the charge transfer signal. In the current device, the working of the qubit is mostly determined by the location of the donor in the y- and z-direction, due to the flat nature of equipotential and equicapacitive surfaces beneath the plunger gate in the x-direction, as observed in Figure 4a. Although the lateral uncertainty of the donor in the x-direction is large (±15 nm), we highlight that it could be narrowed down further by matching donor capacitances obtained from charge stability diagrams involving the barrier and plunger gates. This can also be modeled with FASTCAP, and additional sets of donor loci can be generated. By intersecting the new loci with the current loci, and reducing the experimental error bars on the CTS, we expect that our method could yield a precision better than ±2 nm in all directions.

The range of donor locations amenable to detection via our metrology technique is mostly determined by the tunnel rate between the donor and the SET island, which depends exponentially on their distance. We have used a simple WKB tunnel rate model to estimate this range to be 15−50 nm, obtained by constraining the tunnel times to be between 1 μs and 10 s.

In conclusion, we have applied a combination of classical finite-element and quantum mechanical atomistic techniques to

model the donor electrostatic environment in a spin qubit device based on implanted donors, and we have found a consistent triangulation that pinpoints the donor location to ±2.5 nm in two directions. The accurate knowledge of the location of a donor that has been successfully used to demonstrate an electron spin qubit is of immediate relevance to the design of future devices, where the donor can be deliberately placed in a much more sharply defined volume either by low-energy single-ion implantation through small apertures[19] or by scanning probe techniques.[8] In a broader sense, we highlight that our spatial metrology method could be applicable not only to spin qubit devices, but also to conventional transistors, where cooling down to low-temperature highlights the effect of individual dopants on the conductance of the whole structure.[4] It has been shown that the spin-dependent ionization method can be used to detect the spin resonance of a single electron trapped near the channel of a conventional transistor.[38] Therefore, our method could be applied to extract the location of random dopants in a wide variety of nanoelectronic devices, greatly aiding further efforts toward miniaturization and strategies for deterministic doping.[5]

■ ASSOCIATED CONTENT

Ⓢ Supporting Information

Energy spectrum for phosphorus donors placed at different positions along an equipotential line in the device. This material is available free of charge via the Internet at http://pubs.acs.org.

■ AUTHOR INFORMATION

Corresponding Author
*E-mail: (F.A.M.) fahd.mohiyaddin@student.unsw.edu.au; (A.M.) a.morello@unsw.edu.au.

Present Address
[⊥](R.R.) Network for Computational Nanotechnology, Purdue University, West Lafayette, IN 47907, USA

Notes
The authors declare no competing financial interest.

■ ACKNOWLEDGMENTS

■ REFERENCES

(1) Koenraad, P.; Flatté, M. *Nat. Mater.* **2011**, *10*, 91−100.
(2) Asenov, A.; Brown, A. R.; Davies, J. H.; Kaya, S.; Slavcheva, G. *IEEE Trans. Electron Devices* **2003**, *50*, 1837−1852.
(3) Shinada, T.; Okamoto, S.; Kobayashi, T.; Ohdomari, I. *Nature* **2005**, *437*, 1128−1131.
(4) Pierre, M.; Wacquez, R.; Jehl, X.; Sanquer, M.; Vinet, M.; Cueto, M. *Nat. Nanotechnol.* **2010**, *5*, 133−137.
(5) *International Technology Roadmap for Semiconductors*; 2011; http://www.itrs.net/Links/2011ITRS/Home2011.htm.
(6) Sellier, H.; Lansbergen, G.; Caro, J.; Rogge, S.; Collaert, N.; Ferain, I.; Jurczak, M.; Biesemans, S. *Phys. Rev. Lett.* **2006**, *97*, 206805.
(7) Tan, K.; Chan, K.; Möttönen, M.; Morello, A.; Yang, C.; Donkelaar, J.; Alves, A.; Pirkkalainen, J.; Jamieson, D.; Clark, R.; Dzurak, A. *Nano Lett.* **2010**, *10*, 11−15.
(8) Fuechsle, M.; Miwa, J. A.; Mahapatra, S.; Ryu, H.; Lee, S.; Warschkow, O.; Hollenberg, L. C. L.; Klimeck, G.; Simmons, M. Y. *Nat. Nanotechnol.* **2012**, *7*, 242−246.
(9) Kane, B. E. *Nature* **1998**, *393*, 133−137.
(10) Vrijen, R.; Yablonovitch, E.; Wang, K.; Jiang, H. W.; Balandin, A.; Roychowdhury, V.; Mor, T.; DiVincenzo, D. P. *Phys. Rev. A* **2000**, *62*, 12306.
(11) Hill, C. D.; Hollenberg, L. C. L.; Fowler, A. G.; Wellard, C. J.; Greentree, A. D.; Goan, H.-S. *Phys. Rev. B* **2005**, *72*, 045350.
(12) Hollenberg, L. C. L.; Greentree, A. D.; Fowler, A. G.; Wellard, C. J. *Phys. Rev. B* **2006**, *74*, 045311.
(13) Hollenberg, L. C. L.; Dzurak, A. S.; Wellard, C.; Hamilton, A. R.; Reilly, D. J.; Milburn, G. J.; Clark, R. G. *Phys. Rev. B* **2004**, *69*, 113301.
(14) Morello, A.; Pla, J. J.; Zwanenburg, F. A.; Chan, K. W.; Tan, K. Y.; Huebl, H.; Mottonen, M.; Nugroho, C. D.; Yang, C.; van Donkelaar, J. A.; Alves, A. D. C.; Jamieson, D. N.; Escott, C. C.; Hollenberg, L. C. L.; Clark, R. G.; et al. *Nature* **2010**, *467*, 687−691.
(15) Pla, J. J.; Tan, K. Y.; Dehollian, J. P.; Lim, W. H.; Morton, J. J. L.; Jamieson, D. N.; Dzurak, A. S.; Morello, A. *Nature* **2012**, *489*, 541−545.
(16) Andresen, S. E. S.; Brenner, R.; Wellard, C. J.; Yang, C.; Hopf, T.; Escott, C. C.; Clark, R. G.; Dzurak, A. S.; Jamieson, D. N.; Hollenberg, L. C. L. *Nano Lett.* **2007**, *7*, 2000−2003.
(17) Dupont-Ferrier, E.; Roche, B.; Voisin, B.; Jehl, X.; Wacquez, R.; Vinet, M.; Sanquer, M.; De Franceschi, S. *Phys. Rev. Lett.* **2013**, *110*, 136802.
(18) Kitchen, D.; Richardella, A.; Tang, J.; Flatté, M.; Yazdani, A. *Nature* **2006**, *442*, 436−439.
(19) Jamieson, D. N.; Yang, C.; Hopf, T. F.; Hearne, S. . M.; Pakes, C. I.; Prawer, S.; Mitic, M.; Gauja, E.; Andresen, S. E.; Hudson, F. E.; Dzurak, A. S.; Clark, R. G. *Appl. Phys. Lett.* **2005**, *86*, 202101.
(20) Donkelaar, J. A. V.; Greentree, A. D.; Alves, A. D. C.; Jong, L. M.; Hollenberg, L. C. L.; Jamieson, D. N. *New J. Phys.* **2010**, *12*, 065016.
(21) Ziegler, J. F.; Ziegler, M.; Biersack, J. *Nucl. Instrum. Methods, Sect. B* **2010**, *268*, 1818.
(22) Cerezo, A.; Clifton, P.; Galtrey, M.; Humphreys, C.; Kelly, T.; Larson, D.; Lozano-Perez, S.; Marquis, E.; Oliver, R.; Sha, G.; Thompson, K.; Zandbergen, M.; Alvis, R. L. *Mater. Today* **2007**, *10*, 36−42.
(23) Morello, A.; Escott, C. C.; Huebl, H.; Willems van Beveren, L. H.; Hollenberg, L. C. L.; Jamieson, D. N.; Dzurak, A. S.; Clark, R. G. *Phys. Rev. B* **2009**, *80*, 081307.
(24) Klimeck, G.; Ahmed, S. S.; Bae, H.; Kharche, N.; Rahman, R.; Clark, S.; Haley, B.; Lee, S.; Naumov, M.; Ryu, H.; Saied, F.; Prada, M.; Korkusinski, M.; Boykin, T. B. *IEEE Trans. Electron Devices* **2007**, *54*, 2079−2089.
(25) Klimeck, G.; Ahmed, S. S.; Kharche, N.; Korkusinski, M.; Usman, M.; Prada, M.; Boykin, T. B. *IEEE Trans. Electron Devices* **2007**, *54*, 2090−2099.
(26) Bradbury, F. R.; Tyryshkin, A. M.; Sabouret, G.; Bokor, J.; Schenkel, T.; Lyon, S. A. *Phys. Rev. Lett.* **2006**, *97*, 176404.
(27) Rahman, R.; Wellard, C. J.; Bradbury, F. R.; Prada, M.; Cole, J. H.; Klimeck, G.; Hollenberg, L. C. L. *Phys. Rev. Lett.* **2007**, *99*, 036403.
(28) Nabors, K.; White, J. *IEEE Trans. Comput.-Aided Des. Integr. Circuits Syst.* **1991**, *10*, 1447−1459.
(29) Dehollain, J. P.; Pla, J. J.; Tan, K. Y.; Dzurak, A. S.; Morello, A. *Nanotechnology* **2013**, *24*, 015202.
(30) Pla, J. J.; Tan, K. Y.; Dehollain, J. P.; Lim, W. H.; Morton, J. J.; Zwanenburg, F. A.; Jamieson, D. N.; Dzurak, A. S.; Morello, A. *Nature* **2013**, *496*, 334−338.

(31) Feher, G. *Phys. Rev.* **1959**, *114*, 1219.

(32) Rahman, R.; Park, S. H.; Boykin, T. B.; Klimeck, G.; Rogge, S.; Hollenberg, L. C. L. *Phys. Rev. B* **2009**, *80*, 155301.

(33) *DEVISE, MESH, DESSIS and TECPLOT*, v10.0 Manual; Integrated Systems Engineering (ISE): Zurich, 2004.

(34) McCallum, J. C.; Dunn, M. L.; Gauja, E. *Mater. Res. Soc. Symp. Proc.* **2008**, *1074*, S.

(35) Ahmed, S.; Kharche, N.; Rahman, R.; Usman, M.; Lee, S.; Ryu, H.; Bae, H.; Clark, S.; Haley, B.; Naumov, M.; Saied, F.; Korkusinski, M.; Kennel, R.; McLennan, M.; Boykin, T. et al. In *Encyclopedia of Complexity and Systems Science*; Meyers, R. A., Ed.; Springer: New York, 2009; pp 5745−5783.

(36) Martins, A. S.; Capaz, R. B.; Koiller, B. *Phys. Rev. B* **2004**, *69*, 085320.

(37) Weber, B.; Mahapatra, S.; Watson, T. F.; Simmons, M. Y. *Nano Lett.* **2012**, *12*, 4001−4006.

(38) Xiao, M.; Martin, I.; Yablonovitch, E.; Jiang, H. *Nature* **2004**, *430*, 435−439.

■ NOTE ADDED AFTER ASAP PUBLICATION

References 17 and 30 have been updated. The revised version was re-posted on April 22, 2013.